Separation and Purification Technology 359 (2025) 130368

Contents lists available at ScienceDirect

Separation and Purification Technology

journal homepage: www.elsevier.com/locate/seppur

# Totally conjugated and coplanar covalent organic frameworks as photocatalysts for water purification: Reduction of Cr (VI) while oxidizing water borne organic pollutants

Linyang Wang [a], Jeet Chakraborty [a], Kuber Singh Rawat [b], Maojun Deng [a], Jiamin Sun [a], Yifan Wang [c,d], Veronique Van Speybroeck [b], Pascal Van Der Voort [a,*]

[a] COMOC-Center for Ordered Materials, Organometallics and Catalysis, Department of Chemistry, Ghent University, Krijgslaan 281-S3, 9000 Ghent, Belgium
[b] Center for Molecular Modeling (CMM), Ghent University, Technologiepark 46, 9052 Zwijnaarde, Belgium
[c] Laboratory of Photochemistry, Institute of Chemistry, Chinese Academy of Sciences, Beijing 100190, China
[d] University of Chinese Academy of Sciences, Beijing 100049, China

ARTICLE INFO

Editor: Sergio Obregón

*Keywords:*
Covalent organic frameworks
Photocatalysis
Donor-Accepter alignment
Cr (VI) reduction
High coplanarity

ABSTRACT

Covalent organic frameworks (COFs) have emerged as photocatalytic materials with bandgaps in the visible region. Imine-based COFs, which have been extensively explored, often suffer from limited stability and poor conjugation, hindering their photocatalytic activities. The chemical and hydrolytic stability and the photocatalytic performance of COFs is drastically enhanced by constructing 2D COFs that are fully conjugated in the x, y plane, that have alternating donor–acceptor (D-A) units for better charge separation and that have enhanced conjugation in the z-axis by p-orbital overlap by using highly planar building blocks. In this study, we introduce three highly crystalline $sp^2$ COFs that are able to photocatalyticly reduce highly toxic Cr (VI) species to much less toxic and easily removable Cr (III) residues, while simultaneously oxidizing water borne organic pollutants. One of them, the TEB-COF, with the integration of the acetylene group, exhibited excellent photocatalytic activity due to its superior planarity and extended conjugation. TEB-COF is able to completely remove the model dye Rhodamine B and Cr (VI) (10 mg/L) in less than 30 min. This research provides valuable insights into the development of recyclable metal-free photocatalysts for wastewater treatment.

## 1. Introduction

Water pollution is a critical global problem. In many cases the pollutants are diverse and include both toxic metals and organic compounds. Adsorption or precipitation/flocculation are the most common techniques to remove such pollutants [1–4]. Degradation or functionalization into non-toxic (or less toxic) molecules is an elegant alternative that also neutralizes the sorbed components. Photo-degradation is an interesting technique that is both low-cost and environmentally friendly.

Hexavalent chromium (Cr (VI)) is a common and highly toxic contaminant due to its widespread use in industries such as electroplating, leather tanning, printing, and pigment production [5]. The limitation for total chromium in drinking water is 0.05 mg/L according to the World Health Organization (WHO) [6]. This limit includes the sum of all Cr-species, typically trivalent chromium (Cr (III)) and hexavalent chromium (Cr (VI)). However, Cr (VI) is over 500 times more toxic than Cr (III) [7]. Reduction of Cr (VI) to Cr (III) has another important advantage, since Cr (III) is readily removed, for instance by precipitation as carbonate, sulfide or sulfate. Compared to the more traditional techniques to remove Cr (VI), like membrane separation, chemical reduction, electrolysis, and ion adsorption [5–7], the photocatalytic reduction of Cr (VI) has gained more and more attention [8–10]. Various photocatalysts have been developed for water treatment, including inorganic semiconductors, graphene oxide, and metal–organic frameworks [11–15]. However, many of these photocatalysts have limitations such as poor light-harvesting capabilities, low Cr(VI) reduction efficiency, slow kinetics, or low water stability [16]. Additionally, some metal-based photocatalysts may lead to secondary contamination by leaching heavy metals. Therefore, the development of efficient metal-free photocatalysts is a logical next step.

Covalent organic frameworks (COFs) are excellent porous photocatalysts due to their large surface area, structural regularity, tailorable

* Corresponding author.
*E-mail address:* Pascal.Vandervoort@ugent.be (P. Van Der Voort).

https://doi.org/10.1016/j.seppur.2024.130368
Received 8 September 2024; Received in revised form 17 October 2024; Accepted 1 November 2024
Available online 9 November 2024

functionalities, and strong light-harvesting properties [17,18]. However, most studied COFs in the photocatalytic reduction of Cr (VI) are connected by dynamic bonds. Examples are imine bonds and arylhydrazone bonds, which generally exhibit limited π-electron delocalization and have insufficient chemical stability [19–21]. More stable COFs are vinylene-linked COFs with C═C linkages. They offer important other benefits, such as an excellent in-plane π-electron delocalization throughout the framework, high efficiency in exciton separation, excellent thermal and chemical stability, and a good photocatalytic activity [22]. It is widely recognized that incorporating coplanar backbones and constructing electron donor–acceptor (D-A) structures can improve photocatalytic activity by further extending the π-conjugation, creating local polarization, reducing the exciton binding energy and facilitating electron–hole mobility [23–28]. Thus, the integration of these two strategies should greatly enhance the photocatalytic performance.

So we chose the triazine moiety as the electron accepting building unit because of its planarity, high electron affinity, and conjugated nature [20]. The electron donating building group is the coplanar electron-rich acetylene group [29,30]. In this study, we designed and synthesized

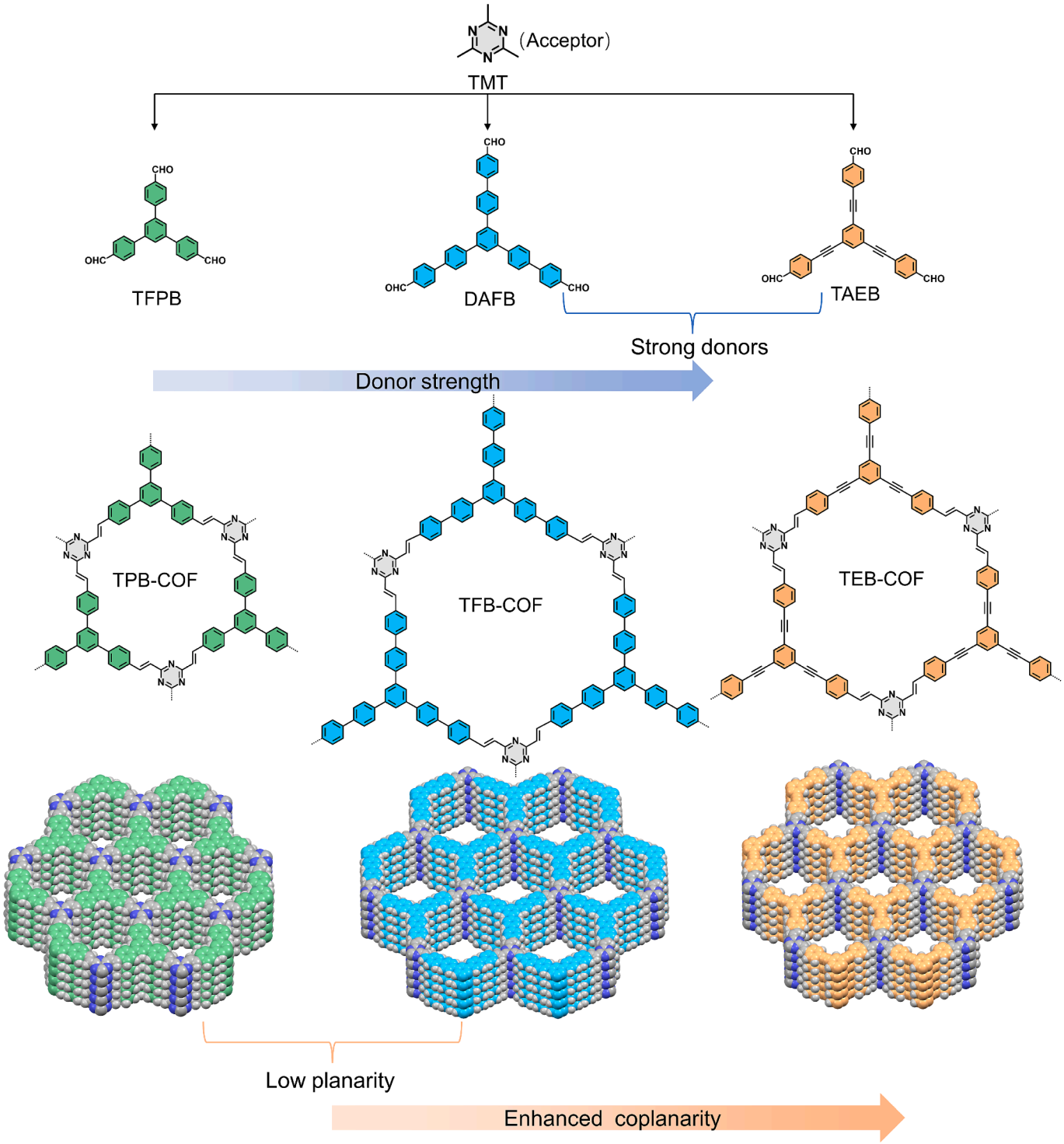


**Fig. 1.** Synthesis scheme for TPB-COF, TEB-COF, and TFB-COF.

three fully conjugated triazine-based 2D COFs, designated as TPB-COF, TEB-COF, and TFB-COF by linking 2,4,6-trimethyl-1,3,5-triazine (TMT) with 5′-(4-Formylphenyl)-[1,1′:3′,1″-terphenyl]-4,4″-dicarbaldehyde (TFPB), 4,4′,4″-(Benzene-1,3,5-triyltris(ethyne-2,1-diyl))-tribenzaldehyde (TAEB), and [1,1:4,1:3,1:4,1-Quinquephenyl]-4,4-dicarboxaldehyde, 5-(4-formyl[1,1-biphenyl]-4-yl)- (DAFB), respectively (Fig. 1). The structure and photochemical properties of the three COFs were comprehensively characterized. The COFs were tested for the photocatalytic reduction of Cr (VI) and simultaneous one pot degradation of dyes under the irradiation of visible light. The D-A structure in TEB-COF proved favorable for the photocatalytic reduction of Cr (VI) and degradation of dyes. Photoelectronic experiments further confirmed the enhanced mobility of charge carriers in TEB-COF.

## 2. Experiment section

### 2.1. Materials and characterization

The chemicals were purchased from TCI Europe or Sigma-Aldrich and used without further purification. X-ray diffraction was carried out on a Bruker D8 Advance diffractometer equipped with a Cu-Kα source (40 kV, 30 mA, λ = 1.5406 Å). Diffuse Reflectance Infrared Fourier Transform Spectroscopy (DRIFTS) measurements were recorded on a Thermo Nicolet 6700 FTIR spectrometer. Nitrogen adsorption experiments were performed on a 3P instrument micropore analyzer. Before the analysis, the samples were degassed at 120 °C for 24 h. The solid UV–vis absorption curve was obtained from the diffuse reflectance spectra (DRS) measured on a Shimadzu UV-3101PC spectrophotometer. $BaSO_4$ was used as the reflectance standard. Luminescence excitation and emission spectra were collected using an Edinburgh Instruments FLSP920 UV–vis-NIR spectrometer setup.The thermogravimetric analyses (TGA) were carried out on a Netzsch STA 449 F3 Jupiter instrument using a heating rate of 10 °C/min in an $N_2$ atmosphere. The isoelectric point was determined using a Malvern Panalytical Zetasizer Ultra, which was equipped for zeta potential measurements. The detection of oxygen was analyzed using a micro-GC (Agilent 990 Micro Gas Chromatograph Micro Gasifier) with Ar (99.99 %) as the carrier gas.

### 2.2. Synthesis of TPB-COF

TPB-COF was synthesized according to reported literature. In detail, TMT (12.3 mg, 0.1 mmol), TFPB (39.04 mg, 0.1 mmol), *n*BuOH (1.4 mL), *o*-DCB (0.6 mL), and KOH (16.8 mg) were placed in an ampoule. The mixture was sonicated for 15 min and then degassed via a freeze–pump–thaw procedure for 3 cycles. The ampoule was flame-sealed and heated at 120 °C for 72 h. The resulting precipitate was collected by filtration, washed with acetone, methanol three times, subjected to Soxhlet extraction with methanol and tetrahydrofuran for 24 h for each solvent, and then dried at 100 °C under vacuum to produce the TPB-COF in 83 % isolated yield.

### 2.3. Synthesis of TEB-COF

TEB-COF was synthesized according to reported literature. In detail, TMT (12.3 mg, 0.1 mmol), TAEB (46.2 mg, 0.1 mmol), mesitylene (0.9 mL), 1,4 −dioxane (0.9 mL), and acetonitrile (0.1 mL) were placed in an ampoule. The mixture was subjected to sonication for 15 min, and then TFAA (0.4 mL) was added. Subsequently, the ampoule was subjected to a freeze–pump–thaw procedure for 3 cycles to remove oxygen. The sealed ampoule was heated at 150 °C for 72 h. The resulting precipitate was collected by filtration, followed by Soxhlet extraction with methanol and tetrahydrofuran for 24 h for each solvent, and then dried at 100 °C under vacuum to produce the TEB-COF in 79 % isolated yield.

### 2.4. Synthesis of TFB-COF

TFB-COF was synthesized according to reported literature. In detail, TMT (12.3 mg, 0.1 mmol), DAFB (61.8 mg, 0.1 mmol), mesitylene (0.9 mL), 1,4 −dioxane (0.9 mL), and acetonitrile (0.1 mL) were placed in an ampoule. The mixture was subjected to sonication for 15 min, and then TFAA (0.4 mL) was added. Subsequently, the ampoule was subjected to a freeze–pump–thaw procedure for 3 cycles to remove oxygen. The sealed ampoule was heated at 150 °C for 72 h. The resulting precipitate was collected by filtration, followed by Soxhlet extraction with methanol and tetrahydrofuran for 24 h for each solvent, and then dried at 100 °C under vacuum to produce the TFB-COF in 81 % isolated yield.

### 2.5. Photocatalytic experiment

In the photocatalytic experiments of Cr (VI) reduction and degradation of organic pollutes, a 300 W Xe lamp with a 420–700 nm wavelength was employed as visible light source. 10 mg of catalyst was dispersed into 30 mL of the reaction aqueous solution under ceaselessly stirring. Prior to light illumination, the reaction suspension was initially stirred under Ar condition for 45 min to reach an adsorption–desorption equilibrium. After a certain time of illumination, the solution was extracted with a 0.22 μm syringe. The absorbance of RhB was detected at 554 nm. The concentration of Cr (VI) was determined by 1,5-diphenylcarbazide method. In 1 mL of the supernatant, 9 mL of sulfuric acid solution (0.2 M) and 0.2 mL of 1,5-diphenylcarbonohydrazide (DPC, 2.5 mg $mL^{-1}$) were added in turn. A purple complex is formed between Cr (VI) and DPC. This reaction has high selectivity for Cr (VI) versus Cr (III). After allowing to stand for 10 min, the absorbance of the Cr (VI)-DPC complex at 540 nm was detected immediately using an UV spectrophotometer.

## 3. Results and discussion

### 3.1. Structural characterization

The three vinylene-linked COFs (TPB-COF, TEB-COF, and TFB-COF) were prepared by linking the aldehyde monomers (TFPB, TAEB, and DAFB) and electron-deficient TMT via the acid-catalyzed solvothermal method (Fig. 1, see Supporting Information for more details). To validate the crystalline structures of the synthesized COFs, powder X-ray diffraction (PXRD) analysis was conducted, and the results are shown in Fig. 2a-c. The TPB-COF showed a sharp peak at $2\theta = 5.8°$, which is assigned to the (1 0 0) plane, and other peaks at 10.4°, 11.8°, 15.7°, and 25.4° are attributed to the (110), (200), (210), and (001) facets, respectively. TEB-COF exhibited five prominent diffraction peaks, with the most intensive one at 4.5° and the four other peaks at 7.9°, 9.3°, 12.4°, and 25.8°, corresponding to the reflections from the planes (1 0 0), (1 1 0), (2 0 0), (210), and (0 0 1), respectively. Similar PXRD pattern could be found for TFB-COF except the peak corresponding to the (100) plane was located at $2\theta = 4.0°$, The shift of the main peak to a lower angle can be attributed to the insertion of the long-chain linker DAFB. Pawley refinements of the simulated AA-eclipsed model against the experimental PXRD pattern of the three COFs were performed using Material Studio. Refined parameters for the unit cell were revealed as $a = b = 17.92$ Å, $c = 3.52$ Å, and $\alpha = \beta = 90°$, $\gamma = 120°$ for TPB-COF; $a = b = 22.12$ Å, $c = 3.63$ Å, $\alpha = \beta = 90°$, $\gamma = 120°$ for TEB-COF; and $a = b = 25.51$ Å, $c = 3.55$ Å, $\alpha = \beta = 90°$, and $\gamma = 120°$ for TFB-COF. High correlation and negligible differences were found between the experimental data and the simulated AA-eclipsed structure ($R_{wp} = 4.25$ % and $R_p = 3.96$ % for TPB-COF; $R_{wp} = 2.62$ % and $R_p = 2.25$ % for TEB-COF; and $R_{wp} = 4.32$ % and $R_p = 2.59$ % for TFB-COF).

In order to confirm the chemical structure of the synthesized COFs, Fourier-transform infrared (FT-IR) analysis was conducted. FT-IR spectra of TPB-COF, TEB-COF, and TFB-COF as well as their corresponding building blocks are shown in Figure S1. A new vibration peak

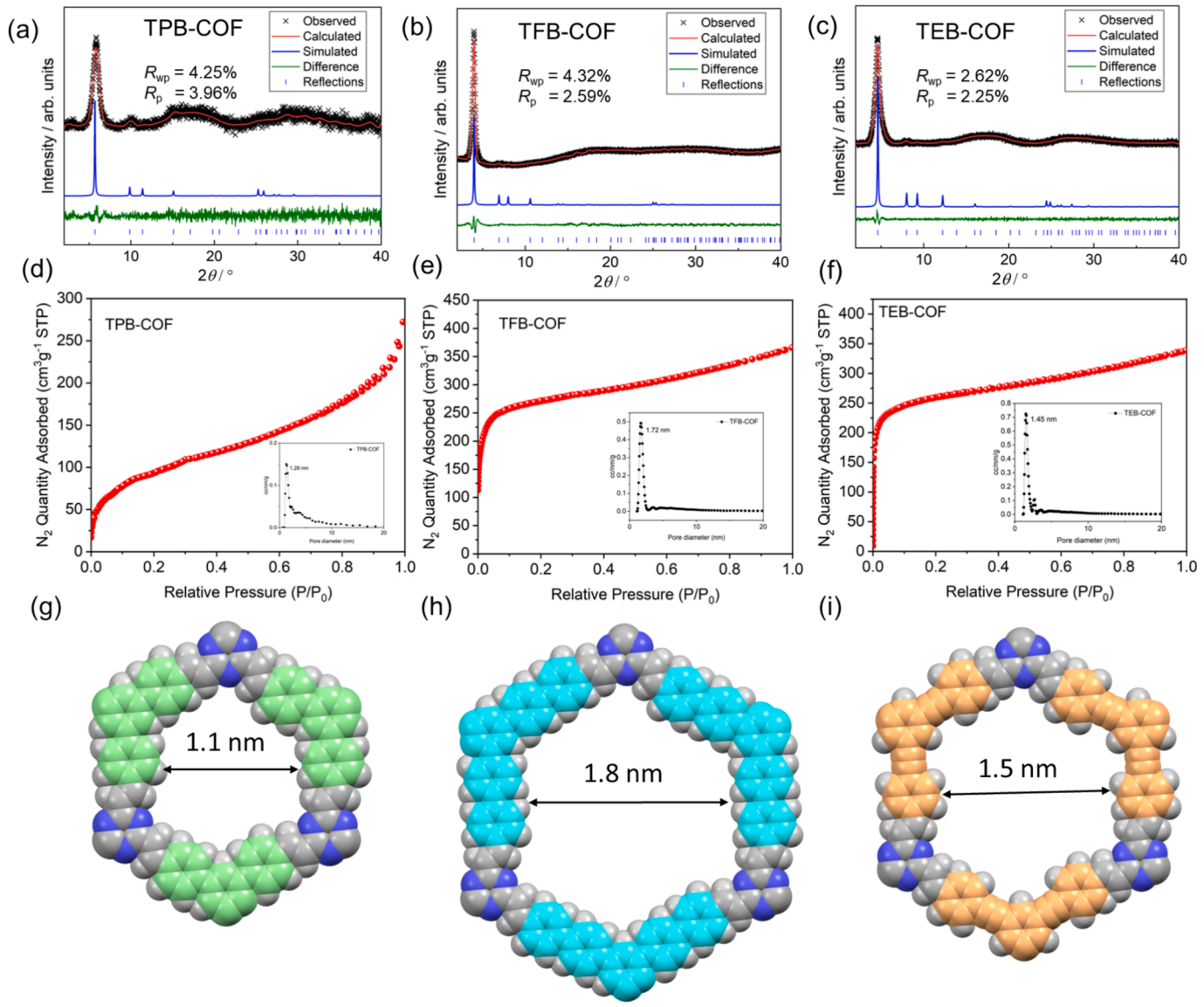


**Fig. 2.** The PXRD patterns and Pawley refinements of (a) TPB-COF, (b) TEB-COF, and (c) TFB-COF in AA stacking modes. $N_2$ sorption isotherms and pore size distributions (inset) of (d) TPB-COF, (e) TFB-COF, and (f) TEB-COF. Images of the crystal structures of the hexagonal structure (g) TPB-COF, (h) TFB-COF, and (i) TEB-COF.

at 1628 $cm^{-1}$ that belongs to the C═C stretching was observed in the FT-IR spectra of the three COFs while lacking in the FT-IR spectra of the monomers, confirming the formation of the vinylene linkages in the three COFs. At the same time, the characteristic absorbance at 1695 $cm^{-1}$ of C═O stretching disappeared in the three COFs, which indicated their high polymerization degree.

The three COFs were further subjected to X-ray photoelectron spectroscopy (XPS) analysis. The XPS survey spectra reveal the presence of C and N elements in all three COFs (Figure S2). The high-resolution C 1s XPS spectrum of TEB-COF (Figure S3a) could be resolved into four peaks with binding energies at 284.5, 285.2, 286.7, and 288.9 eV, which corresponded to C═C ($sp^2$), C≡C (sp), N-C═N in the triazine ring, and π-π*, respectively [31]. The very broad and weak π-π* feature is unspecific and is often associated with shake-up processes, which occur when an electron is ejected from a core level and simultaneously excites another electron to a higher energy state.[35] The high-resolution C 1s XPS spectrum of TFB-COF and TPB-COF (Figure S3b-c) can be deconvoluted into three peaks centering at 284.6, 286.5, and 288.9 eV, which originates from the C═C ($sp^2$), N-C═N in the triazine ring, and π-π*, respectively. TEB-COF, TFB-COF, and TPB-COF (Figure S3d-f) exhibit similar N 1s spectra with a distinct peak around 399.4 eV, assigned to the nitrogen atom in the triazine moiety.

Nitrogen adsorption experiments at 77 K were performed to evaluate the permanent porosity and surface area of these vinylene-linked COFs. As shown in Fig. 2d-f, all three COFs displayed a type-I isotherm indicated by the sharp rise in the low-pressure region ($P/P_0 < 0.05$), suggesting the presence of micropores in the COFs. The surface areas of TPB-COF, TEB-COF, and TFB-COF were calculated to be 265 $m^2\ g^{-1}$, 1150 $m^2\ g^{-1}$, and 1085 $m^2\ g^{-1}$ respectively, by employing the Brunauer-Emmett-Teller (BET) model. The lower surface area of the TPB-COF is mainly due to a lesser crystallinity compared to the two other COFs, which is also apparent from the smaller signal-to-noise ration and the higher Rp value in the XRD patterns. Fitting the $N_2$ adsorption branch data with a quenched solid density functional theory (QSDFT)[32,33] cylindrical pore model resulted in a pore size distribution with prominent distribution peaks at 1.28 nm, 1.45 nm, and 1.72 nm for TPB-COF, TEB-COF, and TFB-COF, respectively, which matched well with the theoretical values (1.1 nm, 1.5 nm, and 1.8 nm) shown in Fig. 2g-i. The total pore volume (at $P/P_0 = 0.99$) of TPB-COF, TEB-COF, and TFB-COF is 0.35 $cm^3\ g^{-1}$, 0.62 $cm^3\ g^{-1}$, and 0.53 $cm^3\ g^{-1}$, respectively.

The thermogravimetric analysis (TGA) was performed to evaluate the thermal stability of the prepared COFs. As illustrated in Figure S4, TEB-COF and TFB-COF showed less than 5 % weight loss up to 400 °C under a nitrogen atmosphere, indicating a good thermal stability. The morphologies of TEB-COF, TFB-COF, and TPB-COF were then examined by scanning electron microscopy (SEM). As shown in Figure S5a-c, TEB-COF and TFB-COF are spherical, whereas the TPB-COF is more fibrous. The chemical stability of the synthesized COFs was assessed by immersing them into common organic solvents (N,N-dimethylformamide, tetrahydrofuran, methanol,) HCl (12 M in water) and NaOH (12 M in water) for three days. There was no significant change in the PXRD pattern (except for TPB-COF that loses some crystallinity in 12 M HCl) after the treatment by different solvents (Figure S6), which indicated their excellent chemical stability.

### 3.2. Optical properties

The optical properties of the as-prepared photocatalysts were investigated by ultraviolet–visible diffuse reflectance spectroscopy (UV–vis DRS). As shown in Fig. 3a, the absorption edges of TPB-COF, TEB-COF, and TFB-COF were observed at 470 nm, 585 nm, and 592 nm, respectively, indicating a strong absorption in both the ultraviolet and visible region. Subsequently, the optical bandgaps calculated from the respective Tauc plots are 2.65 eV, 2.40 eV, and 2.43 eV for TPB-COF, TEB-COF, and TFB-COF, respectively (Fig. 3b). The band structures of the photocatalysts were validated by Mott–Schottky measurements at their corresponding isoelectric points (Figure S7). The flat-band potentials ($E_{FB}$) of TPB-COF, TEB-COF, and TFB-COF are estimated to be –1.10, –0.64, and –0.62 V (vs. Ag/AgCl) at pH = 7, respectively, which convert to standard hydrogen electrode potentials of –0.90, –0.44, and –0.42 V (vs. NHE) at pH = 7. Furthermore, we have indicated the conduction band minimum (CBM) as being the flat band potential –0.1 V, according to Choong and Jang at al.,[34] although opinions on this differ and many papers also use the flat band as the CBM.[35,36] The CBM potential was calculated to be –1.0, –0.54, and –0.52 for TPB-COF, TEB-COF, and TFB-COF, respectively. (Figure S8-10). All three CBMs are more negative than Cr (VI)/Cr (III) (+0.95 V vs. NHE) at pH = 7, indicating that all of them have the potential to facilitate Cr (VI) reduction. Based on the optical bandgaps, the valence bands maximum (VBM) of TPB-COF, TEB-COF, and TFB-COF were calculated to be 1.65, 1.86, and 1.91 V (vs. NHE) at pH = 7, as illustrated in the band-structure diagrams in Fig. 3c.

The capability to effectively separate photoinduced electrons and holes is another crucial factor that influences the catalytic performance of photocatalysts. This capability is often positively correlated with the intensity of the transient photocurrent response (TPR). As depicted in Fig. 3d, the TEB-COF exhibited much higher photocurrent intensity compared to TPB-COF and TFB-COF, suggesting more efficient charge separation in TEB-COF. Moreover, electrochemical impedance spectroscopy (EIS) revealed that TEB-COF possesses the smallest arc radius in the Nyquist plot (Fig. 3e), indicating the lowest interfacial charge transfer resistance. The charge transfer resistance ($R_{CT}$) values after fitting to the Randel circuit were calculated to be 2515 Ω, 816 Ω, and 1733 Ω for TPB-COF, TEB-COF, and TFB-COF, respectively. This trend is in good agreement with the TPR results. Furthermore, photoluminescence (PL) spectra were carried out to assess the efficiency of photoinduced charge separation. As shown in Fig. 3f, upon excitation at 360 nm, the emission peaks of TPB-COF and TFB-COF were approximately located at 570 nm. In contrast, the TEB-COF displayed a redshift of 30 nm, which is attributable to its larger π-extended structure, which lower the energy between the excited state to ground state, leading to longer wavelength. Additionally, the TEB-COF showed significantly lower intensity than TPB-COF and TFB-COF, indicating a reduction of undesired recombination of photo-generated charges, which is favorable to the photocatalytic activity.

### 3.3. DFT calculation

Density functional theory (DFT) calculations were further conducted to understand the effect of chemical structure on the optoelectronic properties of these COFs. All calculations were performed at the PBE-D3 (BJ) level using the VASP package (more details are given in the SI). Our geometry optimization study suggests that the inclined AA-stacking configuration is energetically more favorable than the eclipsed AA-

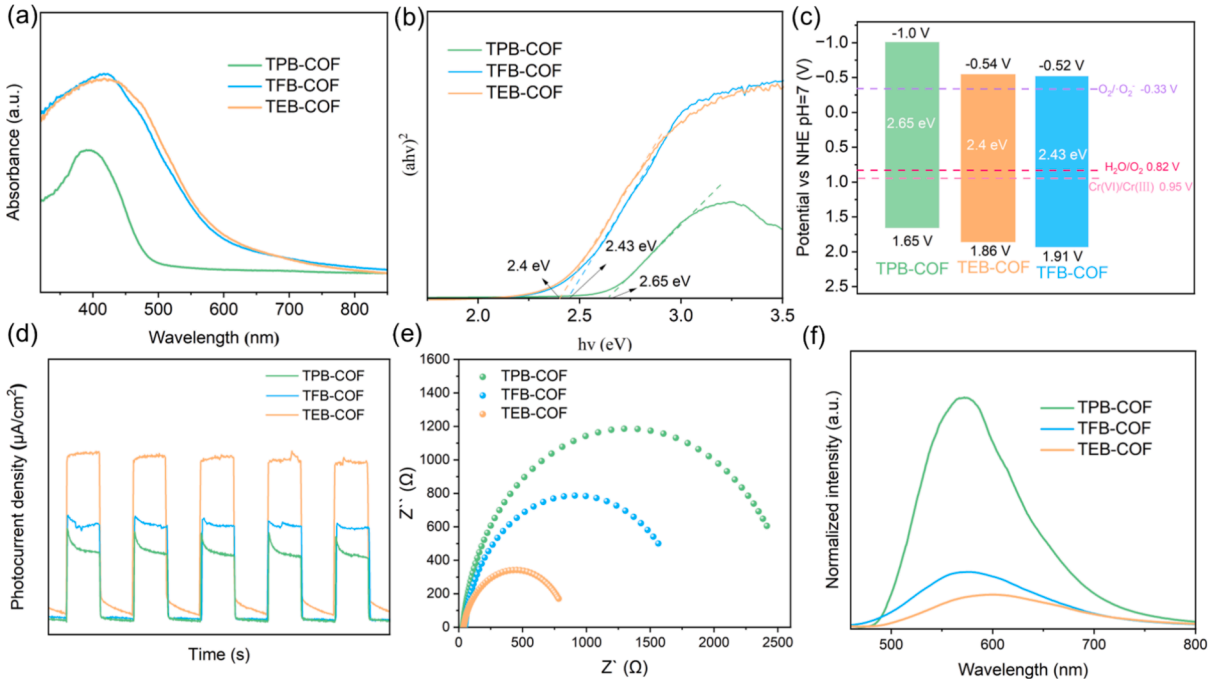


**Fig. 3.** (a) UV–vis DRS spectra of TPB-COF, TEB-COF, and TFB-COF, (b) Bandgaps determined from the Tauc plots, (c) Band-structure diagram, (d) Transient photocurrents under visible light irradiation, (e) electrochemical impedance, and (f) Photoluminescence emission spectra ($\lambda_{ex}$ = 360 nm).

stacking configuration by 0.18 eV, 0.23 eV, and 0.36 eV for TPB-COF, TFB-COF, and TEB-COF, respectively. Therefore, we continue with the inclined AA-stacking for further investigation. The results also show that in TPB-COF and TFB-COF, the strong spatial interactions between hydrogen atoms on neighboring benzene rings induce a twisting of the backbone. This interaction leads to the formation of dihedral angles that reduce the overall planarity of the structure (Fig. 4a). For TPB-COF, the average dihedral angles between the benzene ring and the adjacent triazine ring and between the benzene rings are 10.67° and 17.49°, respectively. In contrast, TFB-COF exhibits increased average dihedral angles of 31.40° and 30.01° between the benzene rings and decreases between the benzene ring and the adjacent triazine ring to 4.58°. However, introducing acetylene building units in TEB-COF eliminates this steric effect, resulting in a highly coplanar structure with a negligible dihedral angle of 2.22°. The highly planar backbone structure has been verified to enhance π-conjugation, thereby accelerating electron separation [26–28].

Fig. 4b shows that TEB-COF has the smallest band gap, aligning well with experimental values. This supports the structural analysis conclusion that TEB-COF's coplanar structure enhances π-π interactions, reducing the band gap. The HOMO (the highest occupied molecular orbital) and LUMO (the lowest unoccupied molecular orbital) value of TFPB, DAFB, and TAEB monomer was calculated to estimate the donor strength of the three linkers. The electron donating ability of a donor monomer is usually related to its HOMO energy level. A high HOMO energy level means that the donor molecule can more easily transfer electrons to the acceptor molecule. As shown in Figure S11, the HOMO values of TFPB, DAFB, and TAEB are calculated to be –7.52, –7.22, and –7.29 eV respectively, indicating the stronger donor ability of TAEB and DAFB monomer. Furthermore, the primary contribution to the HOMO of all three COFs mainly originates from the benzene ring and alkynyl chain (Fig. 4c), whereas the LUMO of TEB-COF and TFB-COF primarily concentrated on the electron-accepting triazine fragment. In contrast, for TPB-COF, it remains distributed over the entire backbone. The reduced overlap between the HOMO and LUMO orbitals in TEB-COF and TFB-COF demonstrates the effective construction of the D-A structure, thereby minimizing charge recombination.

Furthermore, the effective masses (m*) were calculated to evaluate the mobility rate of charge carriers, extrapolated from the calculated band structures (Table 1). The calculated effective electron mass ($m_e^*$) of charge carriers in TEB-COF is significantly smaller than TFB-COF and TPB-COF, indicating faster charge carrier transfer in TEB-COF. Conversely, the effective hole mass ($m_h^*$) of charge carriers is larger for TEB-COF than the other COFs, resulting in a larger difference between

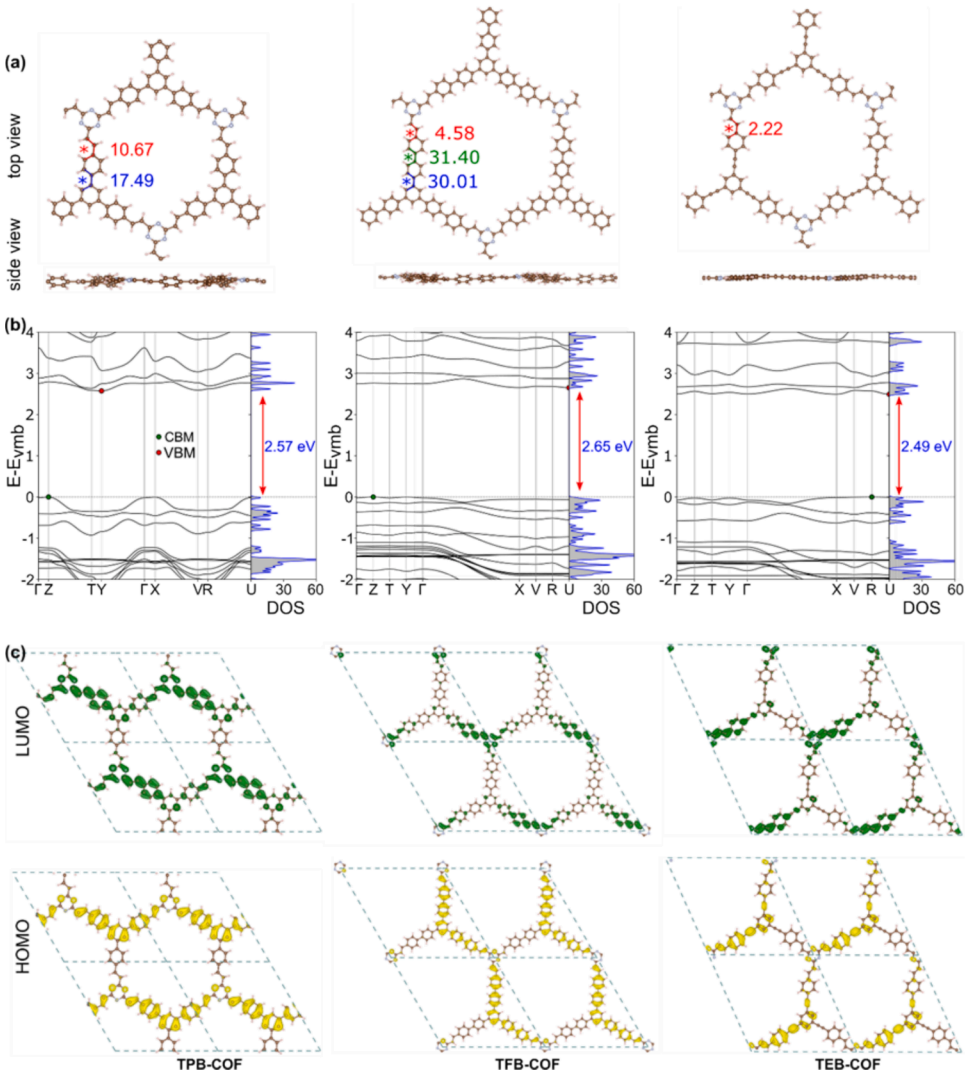


**Fig. 4.** Calculated structural and electronic properties TPB-COF, TFB-COF, and TEB-COF. (a) The top and side view of optimized structures with dihedral angles (°) at the PBE-D3(BJ) level of theory. (b) Band structure and total density of states at HSE06 level of theory and (c) HOMO and LUMO. The valence band maximum (VBM) is shifted to zero and indicated by the grey dashed line, and the VBM and conduction band minimum (CBM) are indicated by red and green dots, respectively.

**Table 1**
Calculated band gap ($E_g$), effective mass of the electron ($m_e^*$) and hole ($m_h^*$) using HSE06 functional. The relative effective mass is defined as $R = m_h^*/m_e^*$. All values of masses are expressed in terms of the free-electron mass $m_0$. The K-points ((Y-T), (Y-G), (U-R) etc.) denote the directions in which the electrons and holes move within the band structure.

| COFs | $E_g$(eV) | $m_e^*$ | $m_h^*$ | $R$ |
|---|---|---|---|---|
| TPB-COF | 2.57 | 8.09 (Y-T)2.289 (Y-G) | −4.15 (Z-G) −1.45 (Z-T) | 0.51 |
| TFB-COF | 2.65 | 1.67 (U-R) | −2.48 (Z-G) −2.13 (Z-T) | 1.48 |
| TEB-COF | 2.49 | 0.77 (U-R) | −10.49 (R-V) −8.226 (R-U) | 13.62 |

the effective masses of holes and electrons. This leads to a larger relative effective mass ratio ($m_h^*/m_e^*$) of TEB-COF indicates its higher carrier separation efficiency.

### 3.4. Photocatalytic performance

The experiments of the photocatalytic reduction of Cr (VI) were carried out under the irradiation of a 300 W xenon lamp (with a 420 nm cut-off filter, to use only visible light). The concentration of Cr (VI) was determined by the 1,4-diphenylcarbazide (DPC) method (see details in supporting information). Prior to the photocatalytic tests, the suspension was stirred for 45 min in dark to reach the adsorption–desorption equilibrium (Figure S12). In the acid condition (pH = 3), the adsorption capacity of TEB-COF for Cr (VI) increases compared to neutral conditions. The calculated equilibrium for adsorbed Cr (VI) is 8.95 mg/g in pH = 3. The results show that only a small fraction of Cr (VI) was adsorbed on the catalyst, confirming the dominant role of photocatalysis in Cr (VI) removal. The photocatalytic performance of the three COFs was assessed by measuring the reducing efficiency of Cr (VI) (10 mg/L) within the same period. As shown in Fig. 5a and Figure S13, after 40 min of irradiation, 99 %, 65 %, and 52 % of Cr (VI) was removed by TEB-COF, TFB-COF, and TPB-COF, respectively (Eq (S1)). TEB-COF exhibits excellent photocatalytic reduction capabilities for Cr (VI) compared to some previously reported porous materials (Table S1). The determination of the reaction rate constant ($k$) can be achieved by using Eq (S2), assuming that the photoreduction of Cr (VI) follows pseudo-first order kinetics.[37,38] As depicted in Figure S14, the $k$ value for TEB-COF was calculated to be 0.092 $min^{-1}$, which is 5.4 times and 4.2 times higher than that of TPB-COF (0.017 $min^{-1}$) and TFB-COF (0.022 $min^{-1}$), respectively. This is a significant discrepancy in the photocatalytic reaction rate between TEB-COF and TFB-COF even though they possess comparable bandgaps, suggesting that the bandgap may not be the primary driver impacting in photocatalytic reduction of Cr (VI). The superior performance of the TEB-COF is attributed to the fact that i) the establishment of a donor–acceptor architecture with the electron deficient triazine moieties and strong electron donating alkynyl building blocks and ii) as show earlier in the manuscript, the TEB-COF is the most coplanar system, with negligible dihedral distortion, as there has the best Z-axis conjugation as well. Both features facilitate the charge separation and charge mobility towards the surface of the catalyst. The effect of initial pH on the photocatalytic reduction of Cr (VI) was investigated and the results are shown in Fig. 5b. When the pH is

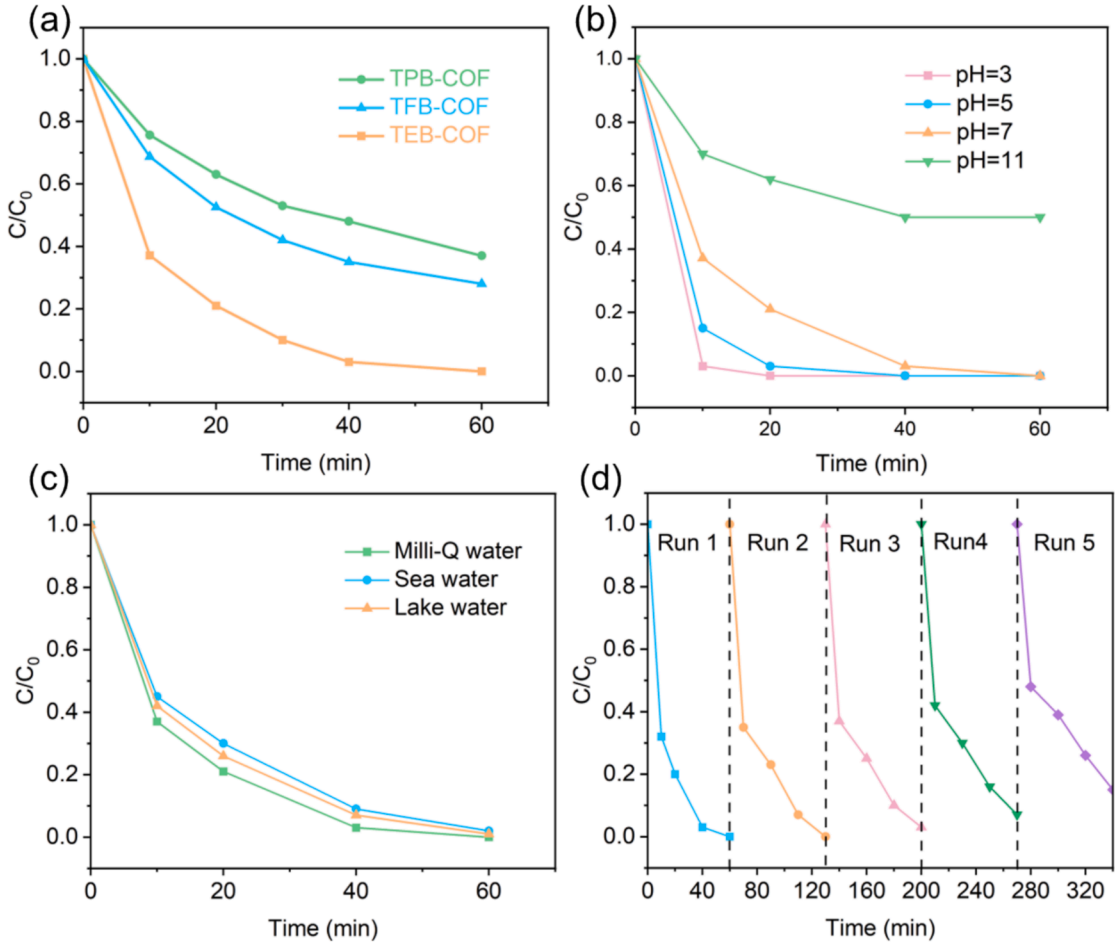


**Fig. 5.** (a) Photocatalytic performance of TPB-COF, TEB-COF, and TFB-COF for the photocatalytic Cr (VI) reduction. The effects of the (b) initial pH, and (c) different water matrix on the photocatalytic Cr (VI) reduction performance of TEB-COF. (d) Recycling tests of TEB-COF in photocatalytic Cr (VI) reduction.

decreases from 7 to 3, the photocatalytic reduction efficiency of Cr (VI) is significantly enhanced. We can explain this as follows: first, the photocatalyst has a positive charge under acidic conditions (Figure S7), which is favorable for the adsorption of the $Cr_2O_7^{2-}$, $CrO_4^{2-}$, and $HCrO_4^-$ anions. Secondly, as the pH decreases, there is a simultaneous increase in the concentration of $H^+$, a crucial reactant in the Cr (VI) reduction reaction under acidic and neutral conditions ($Cr_2O_7^{2-} + 14H^+ + 6e^- \rightleftharpoons 2Cr^{3+} + 7H_2O$).[39,40] On the other hand, under alkaline conditions, the photocatalytic efficiency of Cr (VI) reduction was severely inhibited, resulting in a removal rate of only 40 % after 60 min of irradiation. In alkaline conditions, the catalyst surface is charged negatively (as indicated in the zeta potential plots in Figure S3), resulting in the electrostatic repulsion of the anionic $Cr_2O_7^{2-}$, $CrO_4^{2-}$, and $HCrO_4^-$. Moreover, the reduction of Cr (VI) proceeds as $CrO_4^{2-} + 4H_2O + 3e^- \rightleftharpoons Cr(OH)_3\downarrow + 5OH^-$ under alkaline conditions, The formation of $Cr(OH)_3$ precipitates could obscure active sites on the TEB-COF, leading to the inhibition of the reaction.

We additionally assessed the photocatalytic Cr (VI) reduction efficiency of TEB-COF in seawater and lake water and the results are shown in Fig. 5c. Compared to milli-Q water, the photocatalytic efficiency of TEB in seawater and lake water exhibit negligible changes, which illustrates the feasibility of TEB-COF for practical applications.

The recovery and reuse of catalysts is very important for ecological and economic reasons. Therefore, the reusability of TEB-COF was evaluated by recycling experiments (Fig. 5d). After five consecutive runs, TEB-COF still performed very well with a removal efficiency of over 87 %, demonstrating the good stability of the photocatalyst. The slight decrease in removal efficiency can be mainly attributed to the inevitable weight loss of TEB-COF during the filtration and recycling process, as we work with low masses of photocatalysts.

We also checked the structural features of the spent catalysts after three runs. The crystalline structure of TEB-COF was conserved, as indicated by the PXRD pattern (Figure S16). Moreover, no evident changes were observed in the FT-IR spectrum nor the surface area of the recycled photocatalyst (Figure S17-S18), indicating the robust structural and chemical stability of TEB-COF. As shown in Fig. 6a, the XPS survey spectra of TEB-COF after the photocatalytic reaction (pH = 7) shows the presence of the element Cr, which was not present before the reaction. Additionally, the binding energies of C 1s and N 1s remain consistent with those before the reaction (Fig. 6b-c). The high-resolution Cr 2p spectra of TEB-COF after photocatalytic reaction was composed of two peaks located at 287.2 and 577.3 eV, which are attributed to Cr (III)2p1/2 and 2p3/2, respectively (Fig. 6d) [41,42]. The results of the XPS spectra demonstrate that the Cr (VI) absorbed on the surface of the COF has been efficiently reduced to Cr (III).

### 3.5. Photocatalytic mechanism

In order to shed more light on the photocatalytic mechanism, we performed a series of control and trapping experiments were performed. As shown in Fig. 7a, in the absence of a photocatalyst or light, the concentration of Cr (VI) does not change. When the $O_2$ was replaced with an Ar atmosphere, the efficiency of Cr (VI) reduction decreased very significantly. So oxygen plays a significant role in the reaction,

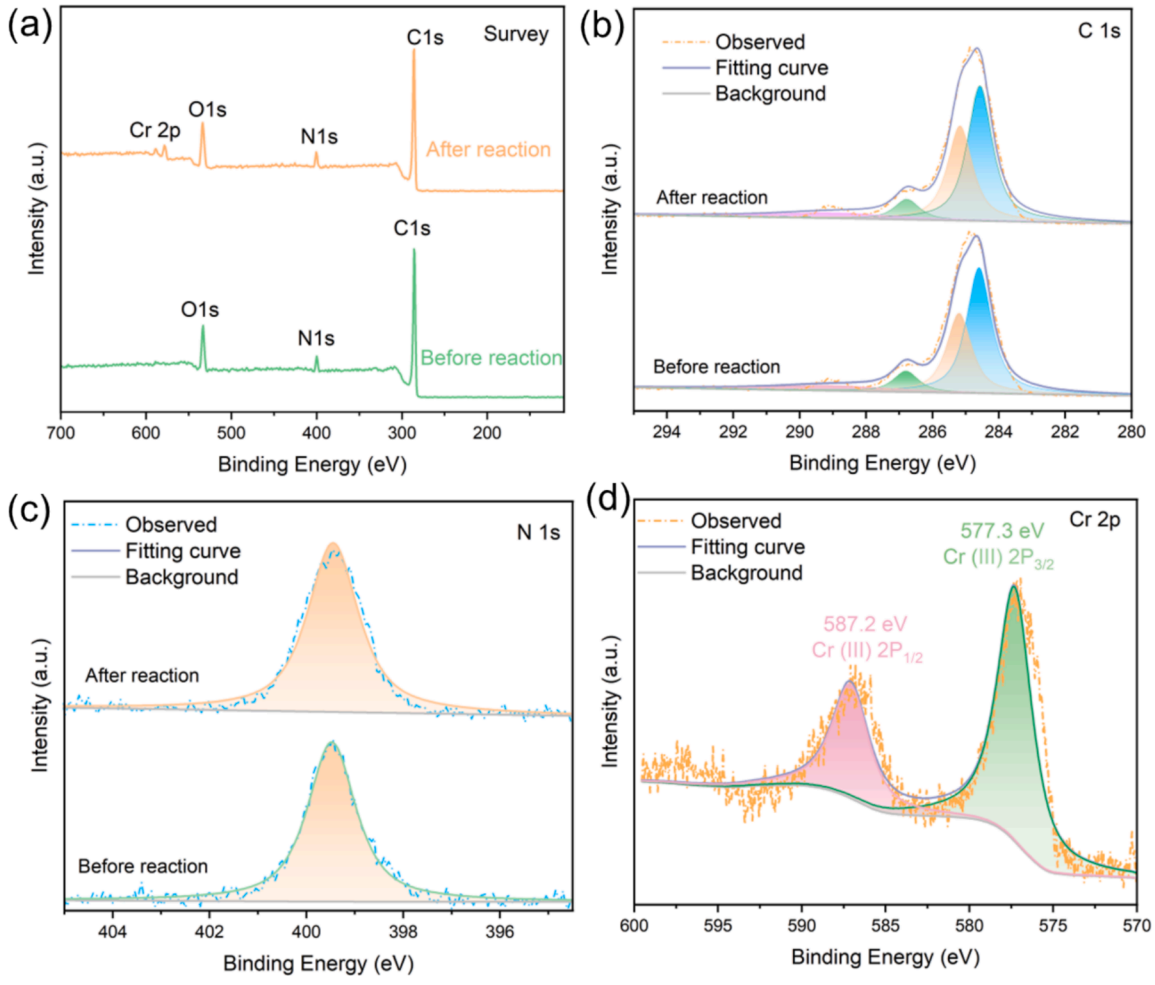


**Fig. 6.** (a) Survey XPS spectrum of TEB-COF, high-resolution spectra of TEB-COF in the region of (b) C 1 s, and (c) N 1 s before and after the reaction. (d) High-resolution XPS spectrum of Cr element on the surface of TEB-COF after the reaction.

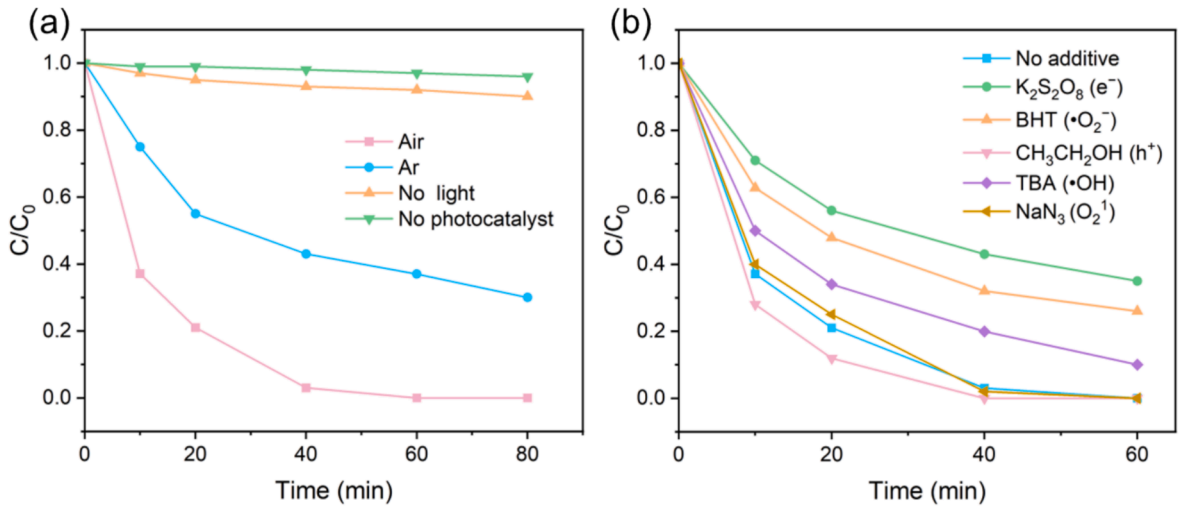


**Fig. 7.** (a) Controlled experiments for the reduction of Cr (VI) under different conditions and (b) trapping experiments with different scavengers.

although the Cr (VI) reduction also seems to proceed through oxygen-free pathways. We also conducted trapping experiments to determine active intermediate species. $K_2S_2O_8$, butylated hydroxytoluene (BHT), sodium azide ($NaN_3$), *tert*-butyl alcohol (TBA), and ethanol ($CH_3CH_2OH$) served as the scavenger of $e^-$, $^{\bullet}O_2^-$, $O_2^1$, $^{\bullet}OH$, and $h^+$, respectively. It can be seen from Fig. 7b that the introduction of $K_2S_2O_8$, TBA, and BHT suppresses the photoreduction of Cr (VI), indicating the $e^-$, $^{\bullet}OH$, and $^{\bullet}O_2^-$ serve as the dominant active species in the photocatalytic reduction of Cr (VI). On the contrary, the capture of holes by $CH_3CH_2OH$ impedes the recombination of photogenerated electron-hole pairs, consequently improving the reaction rate. These results indicate that the main reactive oxygen species (ROS) in the Cr reduction reaction are $^{\bullet}O_2^-$ and $^{\bullet}OH$. The $^{\bullet}OH$ can be formed by reducing $H_2O_2$. We further conducted the $H_2O_2$ measurement to check the pathway of ROS formation. After the photocatalytic Cr (VI) reduction reaction in air condition, we transferred 1 mL of sample solution (after syringe filtration to remove photocatalysts) into a quartz tube and then mixed with 1 mL of Ti reagent solution. Then measure the absorbance of this solution by using UV spectrophotometer. There was an obvious peak at 409 nm, confirming the formation of $H_2O_2$ (see Figure S19). We could not detect $H_2O_2$ after adding the $^{\bullet}O_2^-$ scavenger, indicating that hydrogen peroxide is generated through an indirect two-electron($2e^-$) ORR pathway.

€Based on the band structure of TEB-COF and the radical trapping experiments, a plausible mechanism was proposed in Fig. 9 and Figure S20. Under visible light irradiation, electron-hole pairs (excitons) are generated, that separate into charges that further migrate to the surface of the photocatalyst. The photocatalytic reduction of Cr (VI) typically proceeds through the following three pathways: (i) the photo-excited electrons directly reduce Cr (VI) to Cr (III), (ii) oxygen in the air can also be trapped by electrons to produce superoxide radicals to reduce Cr (VI) indirectly,[43,44] and (iii) The $H_2O_2$ was generated by $^{\bullet}O_2^-$ through two-electron($2e^-$) ORR pathway, the formed $H_2O_2$ further reduce to $^{\bullet}OH$, which participate in the Cr reduction reaction. This was confirmed by the corresponding radical quenching experiment results using $K_2S_2O_8$, TBA, and BHT. For the oxidation reaction, the photoexcited holes oxidize water to produce oxygen. To confirm the oxygen evolution at the VB, a control experiment was performed. $AgNO_3$ was used as an electron scavenger, and the experiment took place in a nitrogen atmosphere to inhibit the oxygen reduction reaction (ORR) while promoting the counter oxidation. Only $O_2$ was observed after 6 h of irradiation, thereby providing evidence for the generation of $O_2$ on the VB of TEB-COF (Figure S21). When ethanol or organic pollutants are present that oxidize more easily than water, the organics will be oxidized without oxygen generation, hereby facilitating the overall redox reaction.

### *3.6. Simultaneous photocatalytic degradation of organic pollutants and Cr (VI) reduction*

We simulated the simultaneous photoreduction of Cr (VI) and the photooxidation of water borne organics, choosing Rhodamine B (RhB) as the model pollutant. We first studied the oxidation half reaction separately. The absorbance wavelength of pure RhB were at 554 nm. As illustrated in Figure S22, the removal efficiency of RhB reach 99 % after 30 min under visible light irradiation. The degradation efficiency of TEB-COF towards RhB is exceptional compared to some previously published porous materials (Table S3).

Similarly, the radicals trapping tests were also conducted at pH = 7 to further investigate the mechanism in photocatalytic RhB degradation (Fig. 8a). In the presence of EDTA-2Na ($h^+$ scavenger) and BHT ($^{\bullet}O_2^-$ scavenger), the degradation efficiency reduced significantly, indicating the dominant role of $h^+$ and $^{\bullet}O_2^-$ in the degradation process. Conversely, the introduction of TBA ($^{\bullet}OH$ scavenger) resulted in only a minor reduction in degradation efficiency, implying that $^{\bullet}OH$ was not the key active species. The results of the trapping experiments revealed that the $h^+$ and $^{\bullet}O_2^-$ were the primary active species responsible for the degradation of RhB.

We subsequently ran the tests of the full system, introducing both the Cr (VI) as the dyes, using the TEB-COF as the active photocatalyst (Fig. 8b). Nearly all RhB was removed within a 20-minute irradiation, at an even faster rate compared to the single half reaction. Similarly, 99 % reduction of Cr (VI) was achieved after 30 min of irradiation, again an improvement of the rate as 50 min were required in the isolated half reaction. This rate increase is due to the fact that the dyes (and most organics) will oxidize easier than water, improving the overall rate of the full redox system. Consequently, the recombination of photo-generated electrons and holes is effectively mitigated, resulting in an enhancement of photocatalytic efficiency.

The photocatalytic mechanism is proposed in Fig. 9, Cr (VI) is reduced to Cr (III) mainly by photo-excited electrons in the CB. On the one hand, electrons can also participate in the reduction of $O_2$ to $^{\bullet}O_2^-$ and $^{\bullet}O_2^- \rightarrow H_2O_2 \rightarrow {}^{\bullet}OH$, thereby further accelerating the photocatalytic reduction of Cr (VI). Organic pollutants (RhB) serve as sacrificial agent to consume the photogenerated holes left in the VB, thus effectively inhibiting photoelectron-hole recombination. Some of the generated $^{\bullet}O_2^-$ is also beneficial for pollutants degradation confirmed by the radical capture experiments.

## 4. Conclusion

We prepared three fully conjugated 2D COFs to perform the

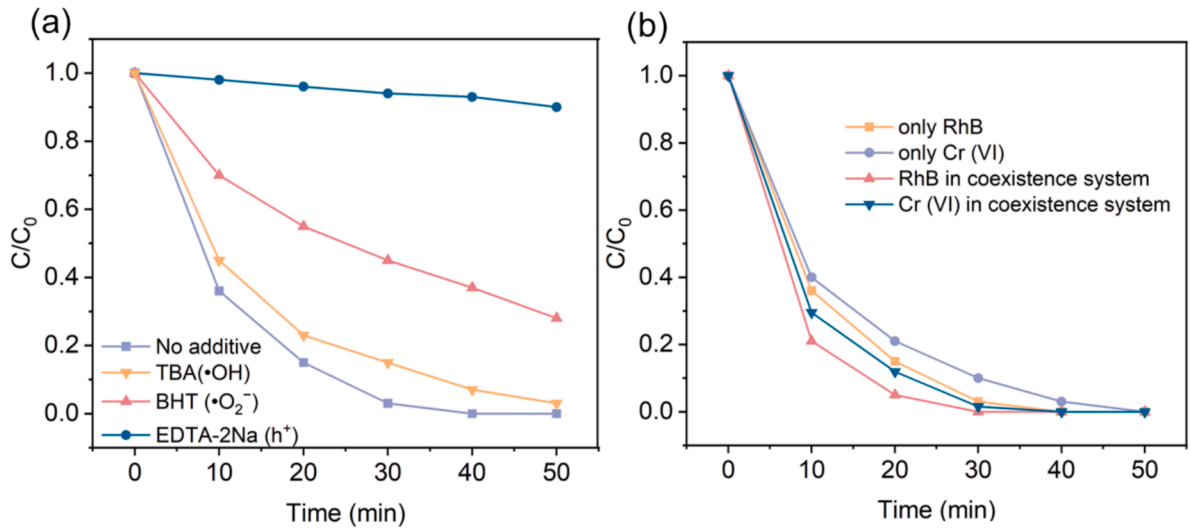


**Fig. 8.** (a) the effect of trapping experiments with different scavenger on photocatalytic degradation of RhB. (b) Comparison of TEB-COF performance for removal of single or mixed pollutants.

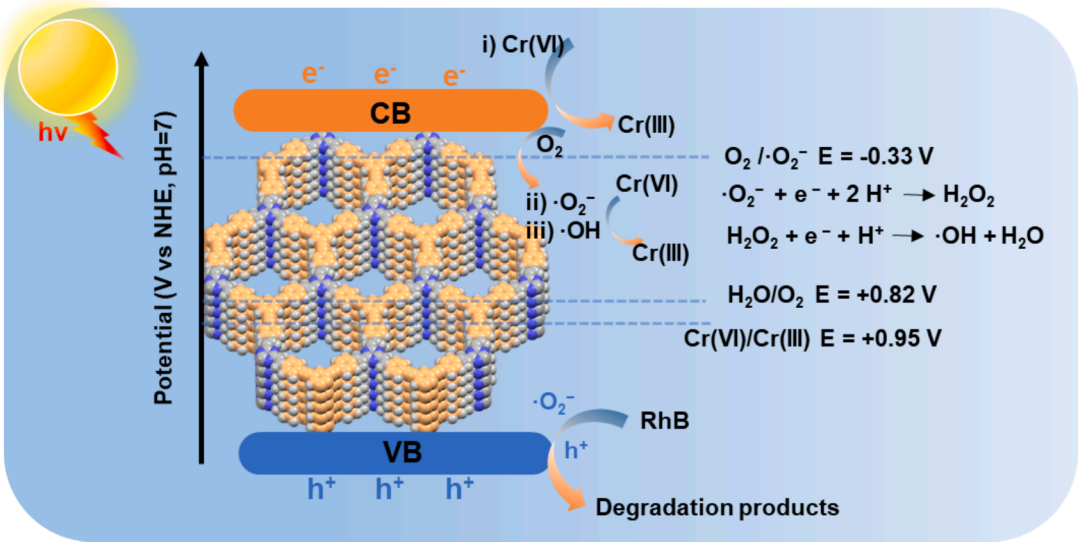


**Fig. 9.** Proposed mechanism for photocatalytic Cr (VI) reduction and organic pollute degradation.

photocatalytic reduction of Cr (VI) with simultaneous degradation of organic pollutes. The very coplanar TEB-COF, based on triazine (acceptor) and acetylene (donor) linkers shows the best performance, due to the fact that the acetylene groups is a strong donor and to the fact that this COFs showed the highest planarity in the z-axis (dihedral angle only 2°), allowing good charge separation and good charge transfer mobility in all 3 dimensions. The oxidation of organics present in the water is not only an efficient pollutant removal strategy, but it also strongly enhances the rate of the Cr (III) reduction due to the favorable oxidation potentials of many organic species. The reduced Cr (III) is easily removed by precipitation techniques. This study exemplifies an effective strategy for the development of durable and metal-free photocatalysts designed for the treatment of water pollutants.

## Author contributions

**Linyang Wang** conceived the idea, designed the experiments and wrote the original draft. Jeet Chakraborty, Maojun Deng, and Jiamin Sun were involved in the validation, investigation and resources. Kuber Singh Rawat conducted the DFT calculation. Yifan Wang conducted X-ray photoelectron spectroscopy (XPS) experiments. **Pascal Van Der Voort** supervised the project and provided assistance with funding acquisition, data analysis and manuscript revision. All authors contributed to discussions and finalizing the manuscript.

## Declaration of competing interest

The authors declare that they have no known competing financial interests or personal relationships that could have appeared to influence the work reported in this paper.

## Acknowledgements

We thank Prof. Dirk Poelman (UGent) for helping with the Solid-state UV-vis measurements. L.-Y. W. (202108110055) and M.-J. D. (202107565003) acknowledge the financial support from the China Scholarship Council (CSC). J. C. acknowledges financial support from UGent (BOF.PDO.2022.0032.01). P. V. D. V. acknowledges the Flemish

Research Foundation (FWO Vlaanderen) for financial support via project G020521N, J.-M. S. acknowledges the financial support from Ghent University (01SC0619) and we also gratefully acknowledge the financial support from the FWO (project I002418N).

## Appendix A. Supplementary data

Supplementary data to this article can be found online at https://doi.org/10.1016/j.seppur.2024.130368.

## Data availability

Data will be made available on request.

## References

[1] S.B. Grant, J.-D. Saphores, D.L. Feldman, A.J. Hamilton, T.D. Fletcher, P.L.M. Cook, M. Stewardson, B.F. Sanders, L.A. Levin, R.F. Ambrose, A. Deletic, R. Brown, S. C. Jiang, D. Rosso, W.J. Cooper, I. Marusic, Taking the "waste" out of "wastewater" for human water security and ecosystem sustainability, Science 337 (2012) 681–686, https://doi.org/10.1126/science.1216852.

[2] C.-C. Wang, X.-D. Du, J. Li, X.-X. Guo, P. Wang, J. Zhang, Photocatalytic Cr(VI) reduction in metal-organic frameworks: a mini-review, Appl. Catal. B Environ. 193 (2016) 198–216, https://doi.org/10.1016/j.apcatb.2016.04.030.

[3] W. Chen, Z. Yang, Z. Xie, Y. Li, X. Yu, F. Lu, L. Chen, Benzothiadiazole functionalized D–A type covalent organic frameworks for effective photocatalytic reduction of aqueous chromium(vi), J. Mater. Chem. A 7 (2019) 998–1004, https://doi.org/10.1039/C8TA10046B.

[4] W.-L. Xue, L. Wang, Y.K. Li, H. Chen, K.X. Fu, F. Zhang, T. He, Y.H. Deng, J.R. Li, C.-Q. Wan, Reticular Chemistry for Ionic Liquid-Functionalized Metal–Organic Frameworks with High Selectivity for CO2, ACS Sustainable Chem. Eng. 8 (2020) 18558–18567, https://doi.org/10.1021/acssuschemeng.0c06551.

[5] U. Divrikli, A.A. Kartal, M. Soylak, L. Elci, Preconcentration of Pb(II), Cr(III), Cu (II), Ni(II) and Cd(II) ions in environmental samples by membrane filtration prior to their flame atomic absorption spectrometric determinations, J. Hazard. Mater. 145 (2007) 459–464, https://doi.org/10.1016/j.jhazmat.2006.11.040.

[6] C.E. Barrera-Díaz, V. Lugo-Lugo, B. Bilyeu, A review of chemical, electrochemical and biological methods for aqueous Cr(VI) reduction, J. Hazard. Mater. 223–224 (2012) 1–12, https://doi.org/10.1016/j.jhazmat.2012.04.054.

[7] Y. Yang, M.h. Diao, M.m. Gao, X.f. Sun, X.w. Liu, G.h. Zhang, Z. Qi, S.g. Wang, Facile Preparation of Graphene/Polyaniline Composite and Its Application for Electrocatalysis Hexavalent Chromium Reduction, Electrochim. Acta, 132 (2014) 496-503. Doi: 10.1016/j.electacta.2014.03.152.

[8] M. Faisal, M. Jalalah, F.A. Harraz, A.M. El-Toni, J.P. Labis, M.S. Al-Assiri, A novel Ag/PANI/ZnTiO3 ternary nanocomposite as a highly efficient visible-light-driven photocatalyst, Sep. Purif. Technol. 256 (2021) 117847, https://doi.org/10.1016/j.seppur.2020.117847.

[9] W. Huang, S. Wang, Q. Zhou, X. Liu, X. Chen, K. Yang, C. Yu, D. Li, Constructing novel ternary composites of carbon quantum dots/Bi2MoO6/graphitic nanofibers with tunable band structure and boosted photocatalytic activity, Sep. Purif. Technol. 217 (2019) 195–205, https://doi.org/10.1016/j.seppur.2019.02.024.

[10] F. Deng, X. Lu, Y. Luo, J. Wang, W. Che, R. Yang, X. Luo, S. Luo, D.D. Dionysiou, Novel visible-light-driven direct Z-scheme CdS/CuInS2 nanoplates for excellent photocatalytic degradation performance and highly-efficient Cr(VI) reduction, Chem. Eng. J. 361 (2019) 1451–1461, https://doi.org/10.1016/j.cej.2018.10.176.

[11] X. Deng, Y. Chen, J. Wen, Y. Xu, J. Zhu, Z. Bian, Polyaniline-TiO2 composite photocatalysts for light-driven hexavalent chromium ions reduction, Sci. Bull. 65 (2020) 105–112, https://doi.org/10.1016/j.scib.2019.10.020.

[12] J. Low, B. Dai, T. Tong, C. Jiang, J. Yu, In situ irradiated X-ray photoelectron spectroscopy investigation on a direct Z-scheme TiO2/CdS composite film photocatalyst, Adv. Mater. 31 (2019) 1802981, https://doi.org/10.1002/adma.201802981.

[13] X. Wang, J. Liu, S. Leong, X. Lin, J. Wei, B. Kong, Y. Xu, Z.-X. Low, J. Yao, H. Wang, Rapid construction of ZnO@ZIF-8 heterostructures with size-selective photocatalysis properties, ACS Appl. Mater. Interfaces 8 (2016) 9080–9087, https://doi.org/10.1021/acsami.6b00028.

[14] G. Fan, X. Zheng, J. Luo, H. Peng, H. Lin, M. Bao, L. Hong, J. Zhou, Rapid synthesis of Ag/AgCl@ZIF-8 as a highly efficient photocatalyst for degradation of acetaminophen under visible light, Chem. Eng. J. 351 (2018) 782–790, https://doi.org/10.1016/j.cej.2018.06.119.

[15] W.-L. Xue, W.-H. Deng, H. Chen, R.-H. Liu, J.M. Taylor, Y.-K. Li, L. Wang, Y.-H. Deng, W.-H. Li, Y.-Y. Wen, G.-E. Wang, C.-Q. Wan, G. Xu, MOF-directed synthesis of crystalline ionic liquids with enhanced proton conduction, Angew. Chem. Int. Ed. 60 (2021) 1290–1297, https://doi.org/10.1002/anie.202010783.

[16] H. Lan, L. Li, H. Liu, X. An, F. Liu, C. Chen, J. Qu, Melem-based derivatives as metal-free photocatalysts for simultaneous reduction of Cr(VI) and degradation of 5-Sulfosalicylic acid, J. Colloid Interface Sci. 507 (2017) 162–171, https://doi.org/10.1016/j.jcis.2017.07.099.

[17] K. Geng, T. He, R. Liu, S. Dalapati, K.T. Tan, Z. Li, S. Tao, Y. Gong, Q. Jiang, D. Jiang, Covalent organic frameworks: design, synthesis, and functions, Chem. Rev. 120 (2020) 8814–8933, https://doi.org/10.1021/acs.chemrev.9b00550.

[18] M.S. Lohse, T. Bein, Covalent organic frameworks: structures, synthesis, and applications, Adv. Funct. Mater. 28 (2018) 1705553, https://doi.org/10.1002/adfm.201705553.

[19] F. Zhang, H. Hao, X. Dong, X. Li, X. Lang, Olefin-linked covalent organic framework nanotubes based on triazine for selective oxidation of sulfides with O2 powered by blue light, Appl. Catal. B Environ. 305 (2022) 121027, https://doi.org/10.1016/j.apcatb.2021.121027.

[20] S. Wei, F. Zhang, W. Zhang, P. Qiang, K. Yu, X. Fu, D. Wu, S. Bi, F. Zhang, Semiconducting 2D Triazine-Cored Covalent Organic Frameworks with Unsubstituted Olefin Linkages, J. Am. Chem. Soc. 141 (2019) 14272–14279, https://doi.org/10.1021/jacs.9b06219.

[21] F. Zhang, X. Ma, X. Dong, X. Miao, X. Lang, Inserting acetylene into an olefin-linked covalent organic framework for boosting the selective photocatalytic aerobic oxidation of sulfides, Chem. Eng. J. 451 (2023) 138802, https://doi.org/10.1016/j.cej.2022.138802.

[22] Z. Li, T. Deng, S. Ma, Z. Zhang, G. Wu, J. Wang, Q. Li, H. Xia, S.-W. Yang, X. Liu, Three-component donor–π–acceptor covalent–organic frameworks for boosting photocatalytic hydrogen evolution, J. Am. Chem. Soc. 145 (2023) 8364–8374, https://doi.org/10.1021/jacs.2c11893.

[23] Z. Fu, X. Wang, A.M. Gardner, X. Wang, S.Y. Chong, G. Neri, A.J. Cowan, L. Liu, X. Li, A. Vogel, R. Clowes, M. Bilton, L. Chen, R.S. Sprick, A.I. Cooper, A stable covalent organic framework for photocatalytic carbon dioxide reduction, Chem. Sci. 11 (2020) 543–550, https://doi.org/10.1039/C9SC03800K.

[24] B.P. Biswal, H.A. Vignolo-González, T. Banerjee, L. Grunenberg, G. Savasci, K. Gottschling, J. Nuss, C. Ochsenfeld, B.V. Lotsch, Sustained Solar H2 evolution from a thiazolo[5,4-d]thiazole-bridged covalent organic framework and nickel-thiolate cluster in water, J. Am. Chem. Soc. 141 (2019) 11082–11092, https://doi.org/10.1021/jacs.9b03243.

[25] N. Keller, D. Bessinger, S. Reuter, M. Calik, L. Ascherl, F.C. Hanusch, F. Auras, T. Bein, Oligothiophene-Bridged Conjugated Covalent Organic Frameworks, J. Am. Chem. Soc. 139 (2017) 8194–8199, https://doi.org/10.1021/jacs.7b01631.

[26] Z.-A. Lan, M. Wu, Z. Fang, X. Chi, X. Chen, Y. Zhang, X. Wang, A fully coplanar donor–acceptor polymeric semiconductor with promoted charge separation kinetics for photochemistry, Angew. Chem. Int. Ed. 60 (2021) 16355–16359, https://doi.org/10.1002/anie.202103992.

[27] M. Xu, C. Wei, Y. Zhang, J. Chen, H. Li, J. Zhang, L. Sun, B. Liu, J. Lin, M. Yu, L. Xie, W. Huang, Coplanar conformational structure of π-conjugated polymers for optoelectronic applications, Adv. Mater. 36 (2024) 2301671, https://doi.org/10.1002/adma.202301671.

[28] F. Zhang, Y. Wang, H. Zhao, X. Dong, X.-K. Gu, X. Lang, Expanding olefin-linked covalent organic frameworks toward selective photocatalytic oxidation of organic sulfides, ACS Appl. Mater. Interfaces 16 (2024) 8772–8782, https://doi.org/10.1021/acsami.3c16838.

[29] S. Jayanthi, D.V.S. Muthu, N. Jayaraman, S. Sampath, A.K. Sood, Semiconducting conjugated microporous polymer: an electrode material for photoelectrochemical water splitting and oxygen reduction, ChemistrySelect 2 (2017) 4522–4532, https://doi.org/10.1002/slct.201700505.

[30] M. Planells, A. Abate, D.J. Hollman, S.D. Stranks, V. Bharti, J. Gaur, D. Mohanty, S. Chand, H.J. Snaith, N. Robertson, Diacetylene bridged triphenylamines as hole transport materials for solid state dye sensitized solar cells, J. Mater. Chem. A 1 (2013) 6949–6960, https://doi.org/10.1039/C3TA11417A.

[31] S. He, B. Wu, Z. Xia, P. Guo, Y. Li, S. Song, One-pot synthesis of gamma-graphyne supported Pd nanoparticles with high catalytic activity, Nanoscale Adv. 5 (2023) 2487–2492, https://doi.org/10.1039/D3NA00096F.

[32] A.V. Neimark, Y. Lin, P.I. Ravikovitch, M. Thommes, Quenched solid density functional theory and pore size analysis of micro-mesoporous carbons, Carbon 47 (2009) 1617–1628, https://doi.org/10.1016/j.carbon.2009.01.050.

[33] W.-L. Xue, P. Kolodzeiski, H. Aucharova, S. Vasa, A. Koutsianos, R. Pallach, J. Song, L. Frentzel-Beyme, R. Linser, S. Henke, Highly porous metal-organic framework liquids and glasses via a solvent-assisted linker exchange strategy of ZIF-8, Nat. Commun. 15 (2024) 4420, https://doi.org/10.1038/s41467-024-48703-5.

[34] H. Kim, C.E. Choong, I. Han, C.M. Park, I.W. Nah, J.R. Kim, B.-H. Jeon, Y. Yoon, M. Jang, Insight into the role of charge carrier mediation zone for singlet oxygen production over rod-shape graphitic carbon nitride: Batch and continuous-flow reactor, J. Hazard. Mater. 424 (2022) 127652, https://doi.org/10.1016/j.jhazmat.2021.127652.

[35] Y.-Z. Cheng, X. Bao, D. Jiang, W. Ji, D.-H. Yang, X. Ding, X. Liu, Y. He, B.-H. Han, Light-promoted extraction of precious metals using a porphyrin-integrated one-dimensional covalent organic framework, Angew. Chem. Int. Ed. n/a (2024) e202414943.

[36] E. Zhou, F. Wang, X. Zhang, Y. Hui, Y. Wang, Cyanide-based Covalent Organic Frameworks for Enhanced Overall Photocatalytic Hydrogen Peroxide Production, Angew. Chem. Int. Ed. 63 (2024) e202400999.

[37] L. Ai, L. Wang, M. Xu, S. Zhang, N. Guo, D. Jia, L. Jia, Defective Bi.333(Bi6S9)Br/Bi2S3 heterostructure nanorods: Boosting the activity for efficient visible-light photocatalytic Cr(VI) reduction, Appl. Catal. B Environ. 284 (2021) 119730, https://doi.org/10.1016/j.apcatb.2020.119730.

[38] L. Zhang, L. Feng, P. Li, X. Chen, Y. Gao, Y. Gong, Z. Du, S. Zhang, A. Zhang, G. Chen, H. Wang, Plasma-assisted doping of nitrogen into cobalt sulfide for loading cadmium sulfide: a direct Z-scheme heterojunction for efficiently photocatalytic Cr(VI) reduction under visible light, Chem. Eng. J. 417 (2021) 129222, https://doi.org/10.1016/j.cej.2021.129222.

[39] Z. Chen, J. Zhao, J. Chen, Y. Zhang, D. Chen, Q. Wang, D. Xia, UiO-66/BiOBr heterojunction functionalized cotton fabrics as flexible photocatalyst for visible-

light driven degradation of dyes and Cr(VI), Sep. Purif. Technol. 258 (2021) 118007, https://doi.org/10.1016/j.seppur.2020.118007.
[40] F. Zhang, Y. Zhang, Y. Wang, A. Zhu, Y. Zhang, Efficient photocatalytic reduction of aqueous Cr (VI) by Zr4+ doped and polyaniline coupled SnS2 nanoflakes, Sep. Purif. Technol. 283 (2022) 120161, https://doi.org/10.1016/j.seppur.2021.120161.
[41] Y.-J. Zhang, J.-L. Ou, Z.-K. Duan, Z.-J. Xing, Y. Wang, Adsorption of Cr(VI) on bamboo bark-based activated carbon in the absence and presence of humic acid, Colloids Surf. A 481 (2015) 108–116, https://doi.org/10.1016/j.colsurfa.2015.04.050.
[42] H. Liu, S. Liang, J. Gao, H.H. Ngo, W. Guo, Z. Guo, J. Wang, Y. Li, Enhancement of Cr(VI) removal by modifying activated carbon developed from Zizania caduciflora with tartaric acid during phosphoric acid activation, Chem. Eng. J. 246 (2014) 168–174, https://doi.org/10.1016/j.cej.2014.02.046.
[43] G. Mo, L. Wang, J. Luo, Controlled thermal treatment of NH2-MIL-125(Ti) for drastically enhanced photocatalytic reduction of Cr(VI), Sep. Purif. Technol. 277 (2021) 119643, https://doi.org/10.1016/j.seppur.2021.119643.
[44] M.B. Hussain, R. Mehmood, U. Azhar, J. Wang, L. Song, BiOCl-Coated UiO-66-NH2 Metal–Organic Framework Nanoparticles for Visible-Light Photocatalytic Cr(VI) Reduction, ACS Appl. Nano Mater. 4 (2021) 4037–4047, https://doi.org/10.1021/acsanm.1c00380.